PAPER

CrossMark
click for updates

Biocompatible CdSe/ZnS quantum dot micelles for long-term cell imaging without alteration to the native structure of the blood plasma protein human serum albumin†

Shanmugavel Chinnathambi,[a] Norhidayah Abu[b] and Nobutaka Hanagata[*ac]

Quantum dots (QDs)—especially those containing cadmium—are toxic to human cells, and therefore cannot be used directly for diagnosis and treatment of human disease. To circumvent this limitation, the surface of QDs must be modified to increase their water solubility and biocompatibility. To this end, we encapsulated CdSe/ZnS QDs coupled with iron oxide nanoparticles in phospholipid micelles ranging in size from 117 to 265 nm. The QD micelles showed no cytotoxicity in A549 and HeLa cells even at higher concentrations (25 μg ml^{-1}). The ability of micelles to transport human serum albumin (HSA) protein was investigated by optical spectroscopy, and the thermodynamic parameters of the protein complexed with micelles were calculated with the van't Hoff equation at various temperatures (25–45 °C). We found that binding between micelles and HSA was stabilized by hydrogen bonds as well as electrostatic and hydrophobic forces. Fourier transform infrared spectroscopy and circular dichroism revealed changes in the secondary structure of HSA due to increment of alpha helical content, although the tertiary structure was largely preserved. The absolute quantum yield of water-soluble micelles was around 4% at an excitation wavelength 590 nm, while that of cadmium selenide (CdSe)/zinc sulfide (ZnS) QDs in chloroform was 20%. The fluorescence signal in HeLa and A549 cells remained high after 72 h of incubation with the micelles, as determined by confocal microscopy; moreover, the fluorescence signal was detected in both mother and daughter cells. These results demonstrate that CdSe/ZnS micelles are biocompatible since they do not induce cytotoxicity during long-term imaging nor affect the native structure of conjugated proteins.

1. Introduction

Fluorescence imaging of biological molecules using probes enables the visualization of cellular morphology and processes.[1] Semiconductor quantum dots (QDs) are a type of probe that have potential therapeutic and biomechanical applications.[2–9] QDs have higher signal intensity than fluorescent proteins and dyes, are photostable, and exhibit tunable emission from visible to infrared wavelengths and extensive absorption coefficients over a broad spectral range. Cadmium-based QDs have demonstrated toxicity in both *in vitro* and *in vivo* studies.[6,7,10,11] This problem can be overcome by modifying the particle surface with water-soluble materials. For instance, phospholipid-modified QD micelles are widely used

in biological applications owing to their low cytotoxicity and high solubility in water.[12–14]

Human blood plasma contains several proteins that are involved in various physiological functions. Serum albumin (SA), the most abundant (60%) protein in blood plasma, maintains blood osmotic pressure and pH, transports endogenous and exogenous molecules (including drugs), and is used as a biomarker for disease diagnosis and treatment. HSA has an ellipsoid shape on highly oriented pyrolytic graphite surfaces, with an average length, width, and height of 12.6, 6.5, and 1.9 nm, respectively, under physiological conditions (pH 7.4).[15] Recent studies have investigated the interaction between functionalized nanomaterials and plasma protein such as SA, fibrinogen, and globulin.[16–20]

In order to establish a safe and efficient system for live cell imaging, in the present study we prepared QDs coated with 1,2-distearoyl-*sn-glycero*-3-phosphoethanolamine-*N*-[biotinyl (polyethyleneglycol)-2000] [DSPE–PEG(2000)–biotin]-terminated phospholipids (Fig. S1†). Biotin is a useful substrate for targeting cancer cells including HeLa and A549 cells, which overexpress biotin receptors such as avidin and streptavidin.[21–23] We also encapsulated oleic acid-terminated iron oxide nanoparticles

aNanotechnology Innovation Station, National Institute for Materials Science, 1-2-1 Sengen, Tsukuba, Ibaraki 305-0047, Japan. E-mail: HANAGATA.Nobutaka@nims.go.jp

bAdvanced Materials Research Centre, SIRIM Berhad, Lot 34, Jalan Hi-Tech 2/3, Kulim, Hi-Tech Park, 09000 Kulim, Malaysia

cGraduate School of Life Science, Hokkaido University, N10W8, Kita-ku, Sapporo, Hokkaido 060-0812, Japan

(Fe_3O_4 NPs) within micelles for the purposes of magnetic separation and magnetic hyperthermia.[24-27] When micelles containing Fe_3O_4 and cadmium selenide (CdSe)/zinc sulfide (ZnS) QDs are taken up by cancer cells, application of an external magnetic field can destroy the cells; moreover, micelle accumulation inside live specimens can be tracked by fluorescence microscopy and QDs can subsequently be removed along with the tumor. Here we investigated the interaction between magnetic CdSe/ZnS QD micelles and HSA as well as the behavior of QD micelles conjugated with HSA in HeLa and A549 cells, including cellular uptake and cytotoxicity.

2. Experimental methods

2.1 Reagents

CdSe/ZnS core shell-type QDs stabilized with octadecylamine ligands were purchased from Sigma-Aldrich (St. Louis, MO, USA; prod. no. 790206-10MG). Fe_3O_4 NPs in chloroform with oleic acid coating was from Nanotech Ocean (San Diego, CA, USA; prod. no. 92126 050412; 25 mg ml^{-1}, 5 nm). DSPE–PEG (2000)–biotin was from Avanti Polar Lipids (Alabaster, AL, USA; prod. no. 880129). Human serum albumin (Product Number 017-10504) was purchased from Wako chemicals (Osaka, Japan). Chloroform and high-performance liquid chromatography (HPLC)-grade water were from Sigma-Aldrich. All chemicals were used without further purification. HeLa (RCB0007) and A549 (RCB0098) cell lines were obtained from Riken Bio-Resource Center (Tsukuba, Japan).

2.2 Preparation of phospholipid encapsulated CdSe/ZnS complexed with Fe_3O_4 NPs

DSPE–PEG (2000)–biotin (10 mg) was dispersed in 1 ml of chloroform; 1.2 mg CdSe/ZnS core shell QDs and 1 mg of a dispersion containing Fe_3O_4 NPs were then added to the phospholipid solution. The mixture was stirred for about 1 h and the chloroform was evaporated in a water bath with a rotary evaporator at 40 °C. The phospholipid film deposited on the reaction vessel was dissolved in 5 ml HPLC water and sonicated for 15 min in a water bath. Resultant micelles were filtered through a 0.2 μm membrane filter (Thermo Fisher Scientific, Waltham, MA, USA). To remove excess lipids from the micelle dispersion, the sample was centrifuged at 15 000 rpm for 10 min, and the pellet was resuspended in HPLC water and re-filtered through a 0.2 μm membrane filter. Magneto fluorescent micelles in 5 ml HPLC water were stored at 4 °C.

2.3 Magnetic separation

Prepared micelles were separated from free phospholipids using a neodymium-based magnet (NdFeB, 50 × 50 × 25 mm) at a magnetic flex density of 0.6 tesla.

2.4 Characterization

High-resolution images were obtained by transmission electron microscopy (TEM) on a G2 F30 S-Twin microscope (FEI Tecnai, Tokyo, Japan) with an acceleration voltage 300 kV. Samples were prepared by drop casting the dispersion onto a carbon-coated

TEM grid. Ultraviolet-visible light (UV-vis) absorption spectra were acquired on a UV-vis spectrophotometer (U-2900; Hitachi, Tokyo, Japan). Photoluminescence spectra were recorded with a spectrofluorometer (Model F-7000; Hitachi) at an excitation wavelength of 500 nm and emission wavelength of 550–750 nm. Excitation and emission slit widths were 5 nm. Samples were loaded in a quartz cuvette for measurements. During photostability measurements, the water/chloroform solution of micelle-encapsulated magnetic CdSe/ZnS and CdSe/ZnS QDs (1 mg ml^{-1}) was illuminated with a UV lamp for 1 h at a wavelength of 365 nm. Vibrating sample magnetometer (VSM) measurements of free Fe_3O_4 NPs and micelles were carried out using a Lake Shore VSM (Lake Shore Cryotronics, Westerville, OH, USA; model no. 7410) at room temperature. Micelle size was determined by dynamic light scattering (DLS) (Otsuka Electronics, Osaka, Japan; model no. DLS 8000) based on the Brownian motion of NPs excited with a He–Ne (632.8 nm) laser. Absolute quantum yields were measured using a C9920-03G system equipped with a 150 W xenon lamp (Hamamatsu Photonics, Hamamatsu, Japan). Measurements were obtained for dilute solutions in 1 cm^2 quartz cuvettes.

2.5 Time-resolved measurements

Fluorescence lifetime measurements were made using a Fluoro Cube UltraFast-3000U time-correlated single photon counting system (Horiba, Hamamatsu, Japan) with a fast-response, red-sensitive photomultiplier tube (Hamamatsu Photonics). The excitation source was a light-emitting diode laser with a wavelength of 570 nm (pulse width ∼ 0.1 ns) and decay measurements were made at 630 nm. The fluorescence emission was detected at a 90° angle relative to the path of the light source. The electrical signal was amplified by a TB-02 pulse amplifier (Horiba) connected to a constant fraction discriminator (Phillips, Amsterdam, The Netherlands). The first detected photon was used as a start signal by a time-to-amplitude converter (TAC), and the excitation pulse triggered the stop signal. The multichannel analyzer recorded repetitive start–stop signals from the TAC and generated a histogram of photons as a function of time-calibrated channels. The instrument response function was obtained using Rayleigh scatter of Ludox-40 (40 wt% suspension in water; Sigma-Aldrich) in a quartz cuvette at 570 nm. Decay analysis software (DAS6V6.0; Horiba) was used to extract lifetime components. The goodness of fit was judged by χ^2 values and by visual observation of the fitted line and residuals. Fluorescence decay was analyzed with two and three lifetimes and χ^2 values were compared to determine the best fit. The time calibration of the system was 6.976663×10^{-12} s per channel. Decays were fitted to the following two-exponent function:

$$F(t) = \sum_{i=1}^{2} a_i \exp(-t/\tau_i) \qquad (1)$$

where $F(t)$ is the normalized photoluminescent decay; a_i normalized amplitudes of decay component τ_i. The average lifetime was calculated from the below equation.

$$\langle \tau \rangle = \sum_{i=1}^{2} a_i \tau_i \qquad (2)$$

2.6 Excitation and emission matrix (EEM)

The EEM was characterized under the following conditions: emission spectra were obtained between 200–600 nm, and the initial excitation wavelength was set to 200 nm in increments of 10 nm. The number of scanning curves was 20 and other scanning parameters were identical to those used for fluorescence emission spectral measurements. For EEM measurements, spectral band passes were maintained at 5 nm for both excitation and emission. Samples were analyzed in 1 ml quartz cuvettes with a 1 cm excitation path length.

2.7 Stocks shift spectroscopy

Synchronous fluorescence spectra were obtained by simultaneously scanning the excitation and emission monochromators at two different constant wavelength intervals – *e.g.*, 15 and 60 nm between excitation and emission monochromators.

2.8 Fluorescence resonance energy transfer (FRET) measurement

The FRET distance and efficiency of energy transfer was calculated from the micelle absorption spectrum and HSA fluorescence spectrum at a concentration ratio of micelles and protein of 1 : 1 at pH 7.4.

2.9 Circular dichroism (CD) measurement

CD spectra of HSA alone and in a micelle complex were obtained with a spectropolarimeter (model J-725; Jasco, Tokyo, Japan) using a 1 mm path length quartz cuvette with a scan speed 100 nm min^{-1}. Ellipticity is expressed in millidegrees. Various micelle concentrations were added as small aliquots of stock solution to protein solutions. Each spectrum represents an average of three scans. Measurements were obtained at 24 °C.

2.10 Fourier transform infrared (FTIR) spectroscopy

Attenuated total reflection FTIR spectra measurements of HSA alone and in a micelle complex were obtained with an FTIR spectrometer (IRTracer-100; Shimadzu, Kyoto, Japan). Spectra of sample and buffer solutions were obtained under the same conditions (pH 7.4).

2.11 Cell cultures

A549 and HeLa cells were cultured in a 75 cm^2 flask for microscopy and the cytotoxicity assay. A549 cells were grown in high-glucose Dulbecco-modified Eagle's medium supplemented with 10% fetal bovine serum, 50 U ml^{-1} penicillin, and 50 mg ml^{-1} streptomycin at 37 °C in humidified air containing 5% CO_2. HeLa cells were cultured under the same conditions but in minimal essential medium.

2.12 Fluorescence microscopy

HeLa and A549 cells (8000 cells per cm^2) were cultured in a 35 mm dish for 24 h for micelle uptake and fluorescence imaging, for which 20 μg ml^{-1} of micelle were used. Control experiments were performed under identical conditions but without adding micelles to the cultures. Cells were washed three times with phosphate-buffered saline and fixed with 3.7% para-formaldehyde for 10 min. Differential interference contrast and fluorescence images were obtained with an SP5 confocal laser scanning microscope (Leica Microsystems, Wetzlar, Germany).

2.13 Cytotoxicity assay

An *in vitro* cytotoxic assay for QDs was carried out using Cell Counting Kit-8 (Dojindo Laboratories, Osaka, Japan). Cells were seeded in a 96-well plate at a density of 5000 per well. QDs were added after 24 h, and the plate was incubated for an additional 24 h followed by incubation with 10 μl cholecystokinin octapeptide for 2 h. Absorbance at 450 nm was measured on a microplate reader (MTP-880Lab; Corona, Hitachinaka, Japan). Cytotoxicity is represented as a percentage of untreated control cells.

3. Results and discussion

3.1 Characterization of micelles containing QDs and magnetic NPs

TEM analysis of free-standing hydrophobic CdSe/ZnS QDs (stabilized with octadecylamine ligands) before surface modification revealed a relatively monodispersed size distribution with an average particle size of 10 nm (Fig. 1A and B). The presence of lattice fringes indicated that the particles were crystalline. We also confirmed the localization of CdSe/ZnS and Fe_3O_4 NPs inside micelles (Fig. 1C and D), which ranged in size from 50 to 70 nm when the two NPs were coencapsulated. The hydrodynamic diameter distribution as measured by DLS revealed a mean micelle diameter of 117.87 ± 2.55 nm. The
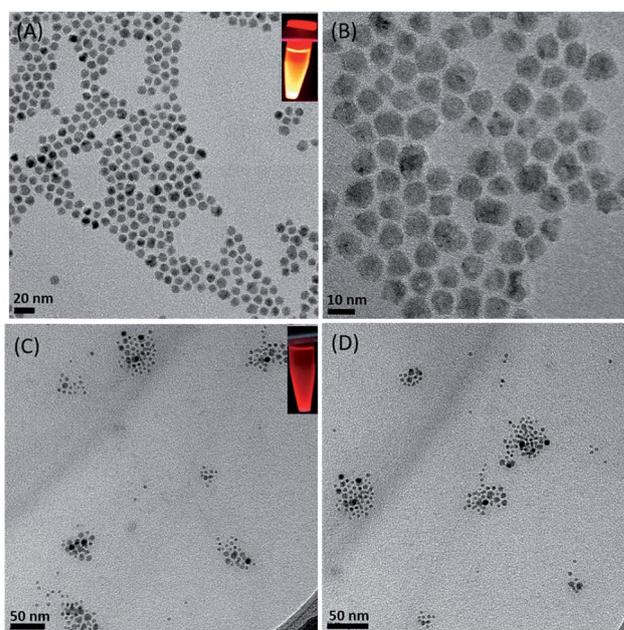

Fig. 1 TEM Characterization. (A, B) CdSe/ZnS QDs with different magnification. (C, D) Magnetic CdSe/ZnS QDs micelles. Inset (A, C) indicates fluorescence under UV light excitation.

ratio of CdSe/ZnS and Fe_3O_4 NPs varied among micelles (Table 1). The presence of CdSe/ZnS and Fe_3O_4 NPs in the micelle core was verified by energy-dispersive X-ray analysis (Fig. S2†). When an external magnetic field was applied to the micelle-containing vessel, the micelle moved to the point where the field gradient was strongest (Fig. S3†); when the magnetic field was removed, the micelle was readily dispersed in water. The micelle showed high luminescence under a magnetic field when excited by UV light.

Fig. 2A shows the absorption spectra of micelle-encapsulated CdSe/ZnS QDs/Fe_3O_4 NPs, CdSe/ZnS QDs in chloroform, and Fe_3O_4 NPs in chloroform. NPs alone had lower absorption than micelles (>500 nm) due to the presence of both NPs inside the micelle core. The fluorescence emission spectra of micelles and CdSe/ZnS QDs were obtained at 630 nm (Fig. 2B); those of micelles and CdSe/ZnS QDs in chloroform were similar. The average lifetime variations of QDs and micelle are shown in Fig. 2C and Table 2. Fe_3O_4 NPs quenched QD fluorescence through energy transfer, reflecting the results from the lifetime profile in the excited state.

Photobleaching is an important parameter in biological imaging experiments. We examined the optical properties of QDs and micelles under irradiation with UV light (Fig. 2D and E). As irradiation time increased, luminescence of the materials decreased due to photobleaching (Fig. 2F). After 60 min of irradiation, the 4% absolute quantum yield of micelles exhibited a stability of 50%, whereas the 20% absolute quantum yield of CdSe/ZnS QD intensity was zero. These results suggest that the prepared micelles are suitable for biological imaging under strong laser illumination or long-term light exposure.

Magnetic characterization was carried out using a VSM. Both QDs and Fe_3O_4 NPs were superparamagnetic at 305 K. Fe_3O_4 NPs alone showed higher magnetization than micelles (Fig. 2G), which had a small amount of these NPs in their core. Nonetheless, upon standardization, the magnetization profile of the two materials were nearly indistinguishable.

3.2 Cytotoxicity of micelle-QDs

Micelles showed no cytotoxicity in the concentration range of 0–25 μg ml^{-1} in HeLa and A549 cell lines exposed for up to 24 h. This may be attributable to the structure of the ZnS shell and phospholipid coating; a previous study reported that a ZnS shell and PEG coating inhibit the release of Cd^{2+} from QDs, which is one known mechanism of QD toxicity. We tested micelles of four different sizes ranging from 117.87 ± 2.55 to 264.66 ± 4.94 nm. In the case of HeLa cells, there was no obvious toxicity

even at higher concentrations, although some effects were observed in A549 cells (Fig. 3A and B).

3.3 Effect of micelle-QDs on serum HSA

Albumin is synthesized in the liver. SA accounts for 55% of blood plasma proteins and maintains osmotic pressure in plasma to enable lipid and steroid hormone transport. Therefore, in order to evaluate the possibility of drug delivery using QD micelles, it is important to clarify the interaction between micelles and HSA. UV-vis spectroscopy is used to study the interaction between NPs and proteins. HSA has absorption peak at 278 nm; we obtained the UV-vis absorption spectrum of HSA in the presence and absence of QD micelles (Fig. 2H). HSA absorption increased in the presence of micelles and showed two bands. The first (∼200 nm) was due to π–π* transition of the polypeptide backbone C=O of HSA, and the second had a peak at 278 nm due to aromatic amino acid residues, especially tryptophan (Trp). The second band changed perceptibly after micelle addition, indicating a change in the microenvironment of the Trp residue. These observations suggest the formation of a ground state complex between HSA and micelles.

The degree of complex formation between HSA and micelles was calculated with the following equation:

$$\text{HSA} + \text{miscelle} \overset{k}{\Leftrightarrow} \text{HSA} : \text{miscelle} \quad (3)$$

where k is an association constant—that is,

$$k = [\text{HSA} : \text{micelle}]/([\text{HSA}][\text{micelle}]) \quad (4)$$

The binding constant of complex formation was determined from the change in intensity of the absorption peak at 278 nm according to the Benesi–Hildebrand relationship:[28]

$$1/(A_{\text{obs}} - A_0) = 1/(A_c - A_0) + 1/K_{\text{app}} [A_c - A_0]1/[\text{micelle}] \quad (5)$$

where A_0 is the absorption of the HSA solution at 1 μM; A is the HSA with increasing concentrations of micelle; and A_c is the final absorption of the conjugated HSA. The plot of $1/(A_{\text{obs}} - A_0)$ against $1/[\text{micelle}]$ was linear (Fig. 2I) and the value of the binding constant K for the HSA–micelle complex was 1.19×10^4 M^{-1}. Complex formation between HSA and micelles was evident from the UV-vis absorption data.

The binding affinity of the micelle–protein interaction was determined by fluorescence emission spectroscopy. The emission maximum of SA was attributable to aromatic amino acids such as Trp, tyrosine (Tyr), and phenylalanine. Trp has a high quantum yield compared to the other aromatic amino acids present in the HSA; Trp214 is located in subdomain IIA, which is the major binding site of HSA. Static or dynamic quenching can occur via FRET, molecular rearrangement, and excited state reactions. When small molecules interact with HSA, the intrinsic fluorescence intensity changes due to Trp residues. Fluorescence emission spectra revealed that adding increasing concentrations of micelle to HSA caused quenching of the protein fluorescence without peak shifts (Fig. 4A), implying that micelles and HSA formed complexes. The polarity of the fluorescence quantum yield surrounding Trp residues was altered

Table 1   DLS values for different sizes of micelle

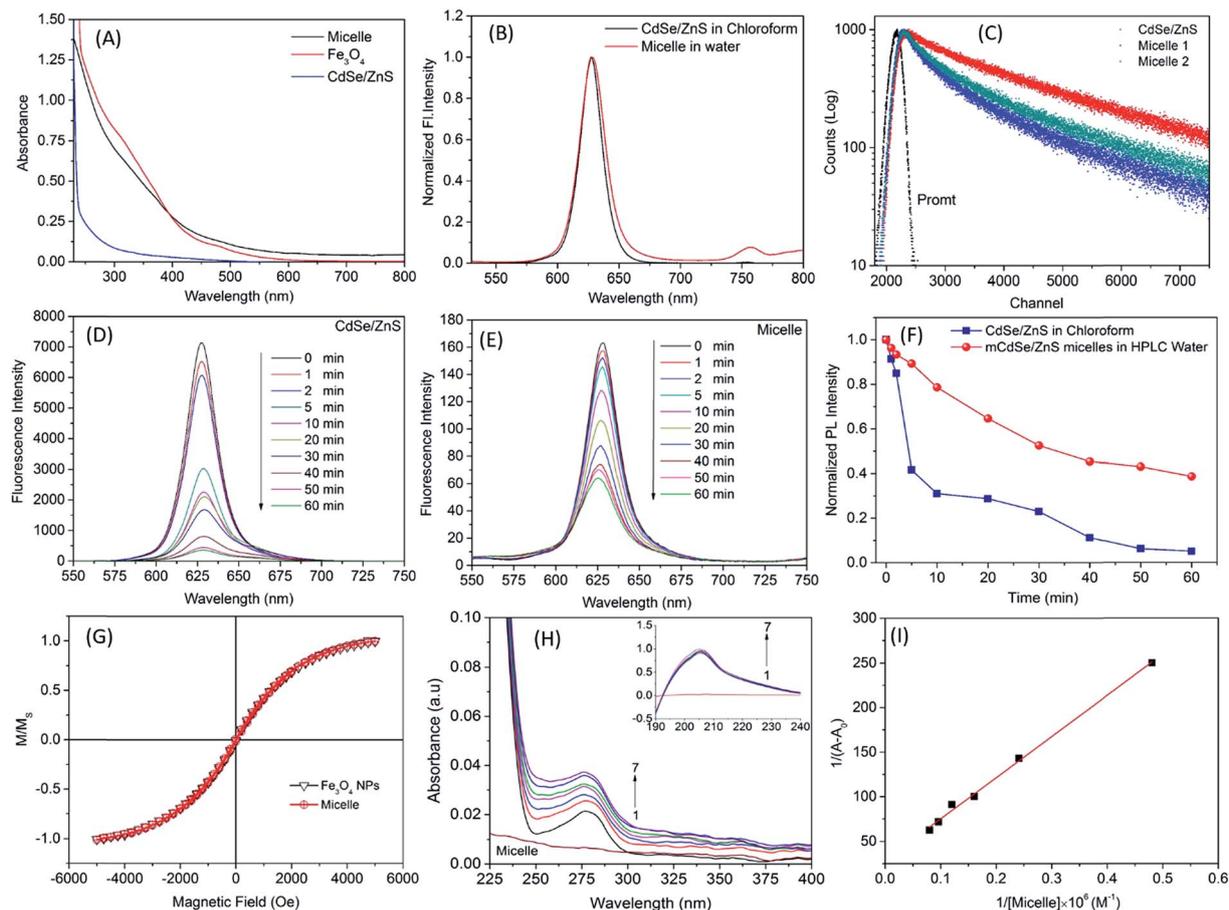| Micelle (CdSe/ZnS) : (Fe$_3$O$_4$)/phospholipid	D_1	D_2	D_3	D_{avg}
M1 (1 : 1)/10 mg	118.5	115.1	120.1	117.87 ± 2.55
M2 (1 : 2)/10 mg	136.9	135.5	130.8	134.40 ± 3.19
M3 (1 : 3)/10 mg	144.9	143.2	138.8	142.30 ± 3.15
M4 (1 : 2)/05 mg	259.4	269.2	265.4	264.66 ± 4.94

Fig. 2 Optical and magnetic characteristics of micelle. (A) UV-vis absorption and fluorescence spectra (B) of micelles with encapsulated CdSe/ZnS QDs and iron oxide (Fe_3O_4) NPs in HPLC water. (C) Time-resolved fluorescence decay profiles of CdSe/ZnS QDs and micelles. Comparison of photostability (F) between CdSe/ZnS QDs (D) and micelles with co-encapsulated CdSe/ZnS and Fe_3O_4 NPs (E). CdSe/ZnS concentrations were similar in both samples (1 mg ml^{-1}) under illumination by 365-nm light. (G) Normalized magnetic moment *vs.* magnetic field for Fe_3O_4 alone and within a micelle. (H) UV-vis spectra of HSA in the absence and presence of different concentrations of micelle (inset shows absorption of polypeptide backbone) and its corresponding Benesi−Hildebrand plot of HSA in the presence of micelle (I).

Table 2 Fluorescence lifetime profiles of CdSe/ZnS QDs and micelles

Samples	α_1	α_2	α_3	τ_1 (ns)	τ_2 (ns)	τ_3 (ns)	τ_0 (ns)	χ^2
CdSe/ZnS	07.39	92.61	—	3.82	19.81	—	19.57	0.96
CdSe/ZnS	09.37	00.76	89.88	5.21	00.86	20.62	20.22	0.95
M1	18.87	81.13	—	2.78	16.48	—	15.96	1.07
M1	22.55	04.41	73.04	4.61	00.89	18.79	17.75	0.99
M2	25.10	74.90	—	2.59	14.69	—	14.01	1.14
M2	28.38	06.01	65.61	4.18	00.84	17.04	15.75	1.04

due to unfolding of the native protein conformation. The decreased quantum yield of Trp214 was due to molecular interaction with micelles.

Fluorescence quenching can be of two types, static and dynamic. The former occurs when molecules (HSA–micelles) form a complex in the ground state, and the latter when molecules come into contact during the transient existence of the excited state. To confirm whether HSA–micelle complexes exhibit static or dynamic quenching, we plotted F_0/F *vs.* [Q];

a linear relationship was observed (Fig. 4B), providing evidence for static quenching.

The K_q was calculated using the Stern–Volmer equation, which is expressed as follows:[29–31]

$$\frac{F}{F_0} = 1 + K_{sv}[Q] = 1 + K_q\tau_0[Q] \qquad (6)$$

where F and F_0 are the fluorescence intensities in the presence and absence of micelles (quencher), [Q] is the quencher concentration, K_{sv} is the Stern–Volmer quenching constant, K_q is the bimolecular quenching rate constant, and τ_0 is the lifetime of the fluorophore in the absence of quencher. The average lifetime of HSA was $\tau_0 = 5.89$ ns; at 298 K, $K_q = 5.67 \times 10^{12}$ l mol^{-1} s^{-1}, which was two orders of magnitude higher than that of a purely dynamic quenching process. This suggests that the fluorescence quenching of HSA by micelles is due to static ground state complex formation.

To clarify the dynamics of the HSA–micelle complex, we measured the fluorescence lifetime of HSA in the presence and absence of micelles (Fig. 4). HSA alone showed a biexponential
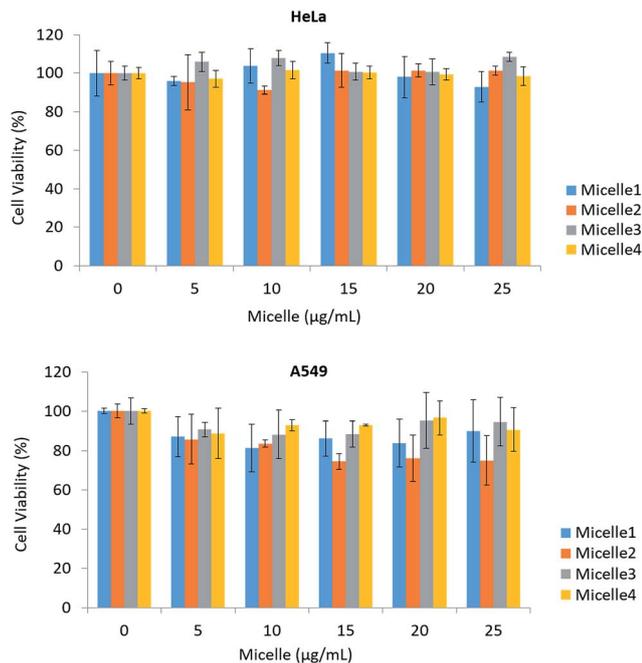
Fig. 3 Toxicity of micelles encapsulating magnetic CdSe/ZnS QDs. HeLa and A549 cells were incubated with micelles for 24 h. Sizes of the micelle used in this test: Micelle 1 (117.87 ± 2.55 nm), Micelle 2 (134.40 ± 3.19 nm), Micelle 3 (142.30 ± 3.15 nm) Micelle 4 (264.66 ± 4.94 nm).

decay curve with an average lifetime of 5.89 ns and lifetime components of 27.86% and 72.14%. The fluorescence decay of HSA was unaltered by increasing micelle concentrations (Table 4), remaining biexponential in the presence of 42 μg micelle with an average lifetime 5.80 ns and lifetime components of 26.29% and 73.71%, respectively. Minute alterations

occurred as a result of changes in the local conformation of HSA. A time-resolved Stern–Volmer plot was generated with the following equation:[32]

$$\frac{\tau_0}{\tau} = 1 + K_{sv}[Q] \tag{7}$$

where the average lifetime, $\tau = \sum a_i \tau_i$.

The plot was parallel to the x axis, indicating a static quenching mechanism for the interaction between the micelle and HSA (Fig. 4D). Trp214 was located in the hydrophobic cavity of subdomain IIA, which is where the micelle was bound, resulting in quenching.

We calculated binding parameters at different temperatures using the van't Hoff equation to determine the driving force between micelles and HSA (Fig. 5):[33]

$$\ln K = \frac{\Delta S}{R} - \frac{\Delta H}{RT} \tag{8}$$

where K is the association constant, T is the absolute temperature, and R is the gas constant (8.3145 J mol^{-1} K^{-1}). From the van't Hoff plot, we calculated enthalpy and entropy changes (ΔH and ΔS, respectively) between $\ln K$ and $1/T$. The free energy change (ΔG) of the reaction at different temperatures was calculated using ΔH and ΔS in the equation $\Delta G = \Delta H - T\Delta S$. The binding parameters are listed in Table 3. The ΔG value was more negative due to negative ΔH and positive ΔS values, thus favoring micelle–HSA complex formation. Positive values of ΔH and ΔS indicate hydrophobic interactions, whereas negative values indicate van der Waal's forces and hydrogen bond formation.[34] A positive ΔS and negative ΔH suggest a specific electrostatic interaction between specific ions in an aqueous solution. The negative change in enthalpy ($\Delta H° = -119.90$ kJ mol^{-1}) and positive change in entropy ($\Delta S° = 11.12$ J mol^{-1} K^{-1}) values for HSA–micelle binding indicate an entropy-driven
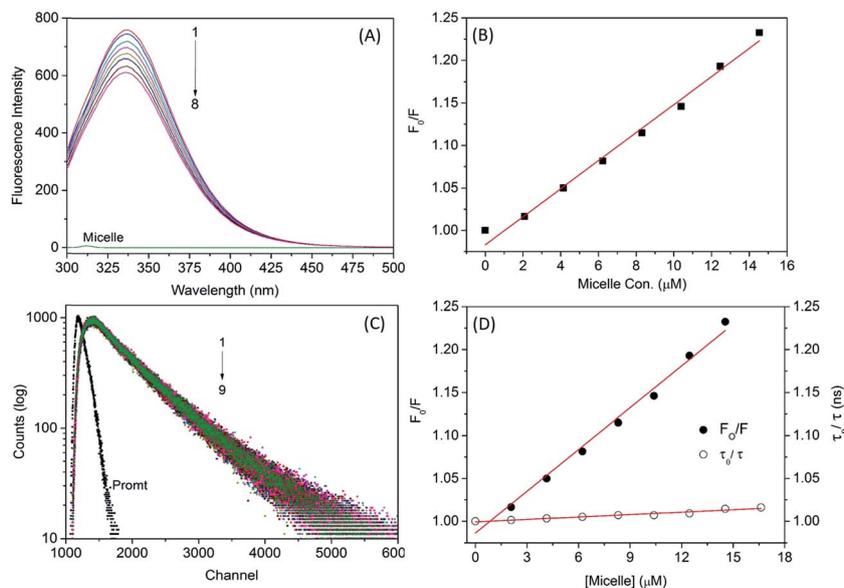

Fig. 4 HSA fluorescence quenching by micelle. Fluorescence steady (A) and excited state (C) quenching spectra of HSA in the absence and presence of different concentrations of micelle. (B) Steady state Stern–Volmer plot (D) overlap graph of steady state and excited state Stern–Volmer plots.
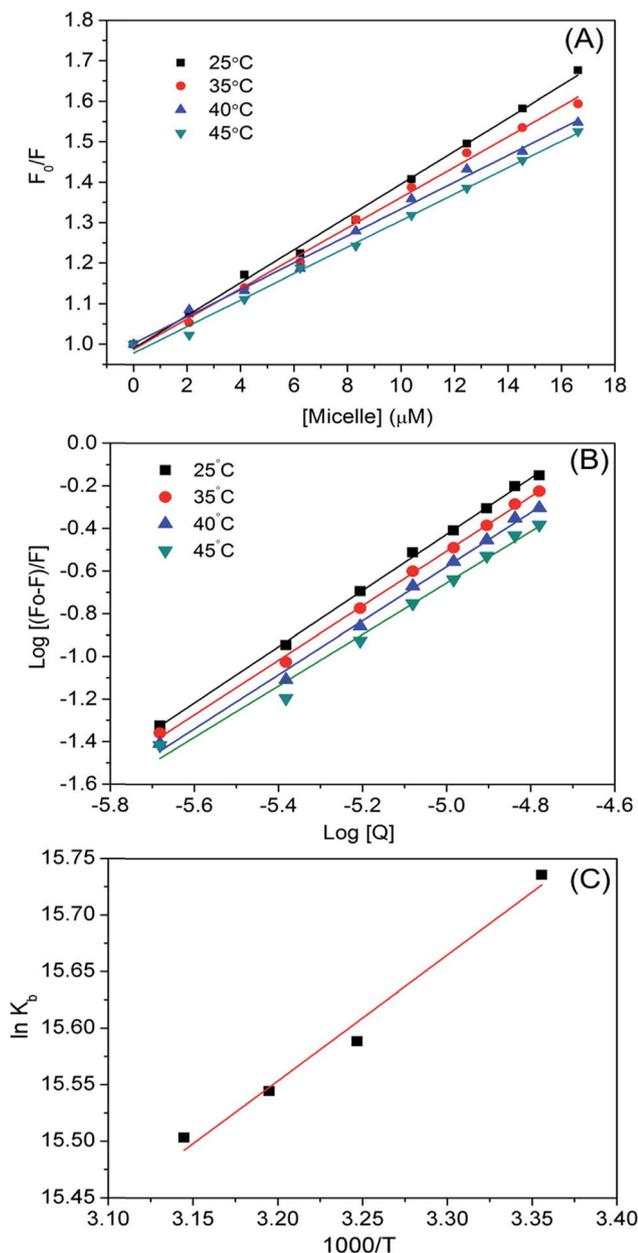
Fig. 5 Effect of temperature on the HSA–micelles association. (A) Steady-state Stern–Volmer plots at different temperatures. (B) Effect of temperature on the binding constant between HSA and micelles. (C) van't Hoff plot for the HSA–micelle complex.

Table 4 Fluorescence lifetime profiles of HSA alone and complexed with micelles

Sample	α_1	α_2	τ_1 (ns)	τ_2 (ns)	τ_0 (ns)	χ^2
1	27.86	72.14	2.52	6.41	5.8972	1.01
2	28.61	71.39	2.53	6.42	5.8894	1.04
3	27.17	72.83	2.46	6.37	5.8776	1.03
4	28.26	71.74	2.58	6.39	5.8671	1.05
5	27.14	72.86	2.54	6.35	5.8559	1.08
6	23.99	76.01	2.34	6.27	5.8558	1.10
7	26.13	73.87	2.45	6.31	5.8438	1.08
8	24.65	75.35	2.36	6.24	5.8127	1.08
9	26.29	73.71	2.42	6.27	5.8041	1.13

whereas ΔH values are either close to zero or negative for a number of processes involving hydrophobic interactions. Binding of ligand to protein buries the water-accessible surface area and thereby releases the solvent from the surface. A positive ΔS value reflects the associated entropic changes in the system and indicates that the interaction between the micelle and HSA is hydrophobic. Thus, hydrophobic effects, electrostatic forces, and hydrogen bonding predominate the micelle–HSA interaction. Possible micelle–HSA assemblies are illustrated in Fig. S4C.†

We used three dimensional fluorescence spectroscopy to further examine the conformational changes in HSA induced by addition of micelles (Fig. 6). Peaks 1 and 2 represent fluorescence from HSA, and peaks x and y correspond to Rayleigh and second order-scattering peaks, respectively. Peak 1 arises from the intrinsic fluorescence of HSA due to Tyr and Trp (tertiary structure) residues participating in the $\pi \rightarrow \pi^*$ transition, whereas peak 2 was attributable to fluorescence characteristics of the polypeptide backbone structure (secondary structure) of HSA caused by $\pi \rightarrow \pi^*$ transition. These peaks are associated with HSA fluorescence quenching upon binding with micelles.

Conformational changes in the microenvironment around the fluorophores Tyr ($\Delta\lambda = 15$ nm) and Trp ($\Delta\lambda = 60$ nm) were determined based on synchronous fluorescence spectra obtained for HSA at increasing concentrations of micelle (Fig. 7A and B). A small red shift of 2 nm was detected within the maximum emission for Tyr, while there was no shift for Trp, suggesting that micelle–HSA binding had altered the microenvironment of Tyr but not Trp residues—specifically, a shift from a nonpolar, hydrophobic environment to one that is more hydrophilic.

3.4 Secondary structure of HSA

We monitored the secondary structure of the HSA interaction with QD-containing micelles by CD spectroscopy (Fig. 7C).

interaction in which enthalpy is unfavorable, resulting in the stabilization of a specific electrostatic force. A negative ΔH value could also represent hydrogen bonding. ΔS values are positive

Table 3 Fluorescence binding parameters for HSA–micelles

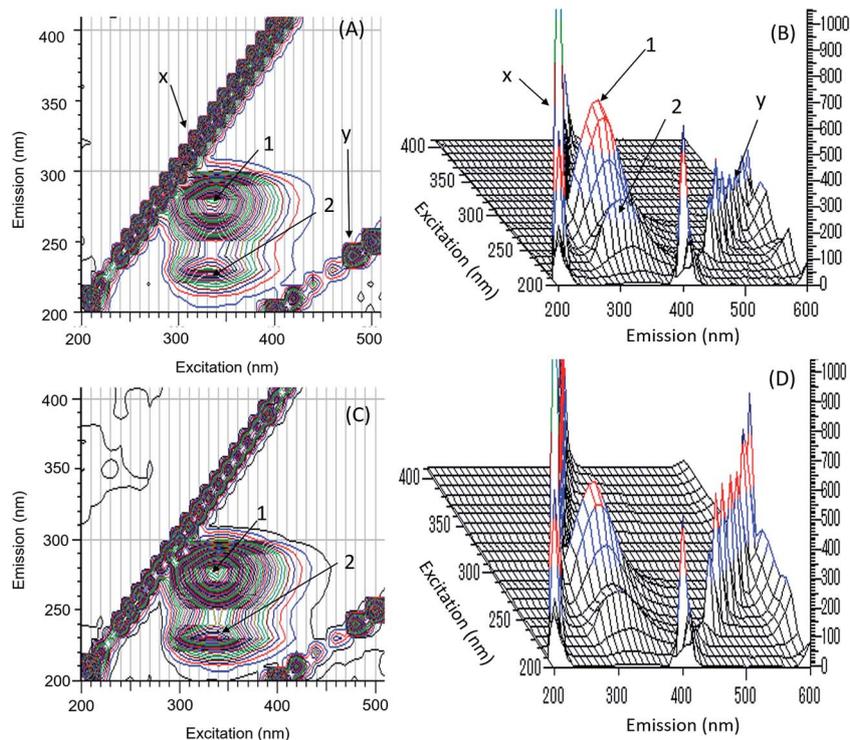| T (°C)	K_q ($\times 10^{12}$ l mol^{-1} s^{-1})	K_b ($\times 10^6$ l mol^{-1})	n	R^2	$\Delta G°$ (kJ mol^{-1})	$\Delta H°$ (kJ mol^{-1})	$\Delta S°$ (J mol^{-1} K^{-1})
25	5.67	6.16	1.31	0.99	−35.719	−119.90	11.12
35	5.61	5.89	1.27	0.99	−36.918		
40	4.48	5.75	1.26	0.99	−37.517		
45	4.11	5.37	1.20	0.98	−38.117		

Fig. 6 Contour map and three dimensional fluorescence spectra of interaction of HSA in the absence (A, B) and the presence (C, D) of micelles.

Native HSA contains two negative peaks at 208 and 222 nm and has an α-helical content of 67.45% ± 0.73%.[32,35] After serial addition of micelles at concentrations of 2, 4, and 6 μM, the α-helical content increased to 70.05% ± 0.81%, 72.24% ± 0.77%,

and 74.11% ± 0.68%, respectively. However, the shape and positions of the protein peaks were unaltered in the presence of micelles. Thus, the increment in the α-helical content changed the secondary structure of protein during interaction with
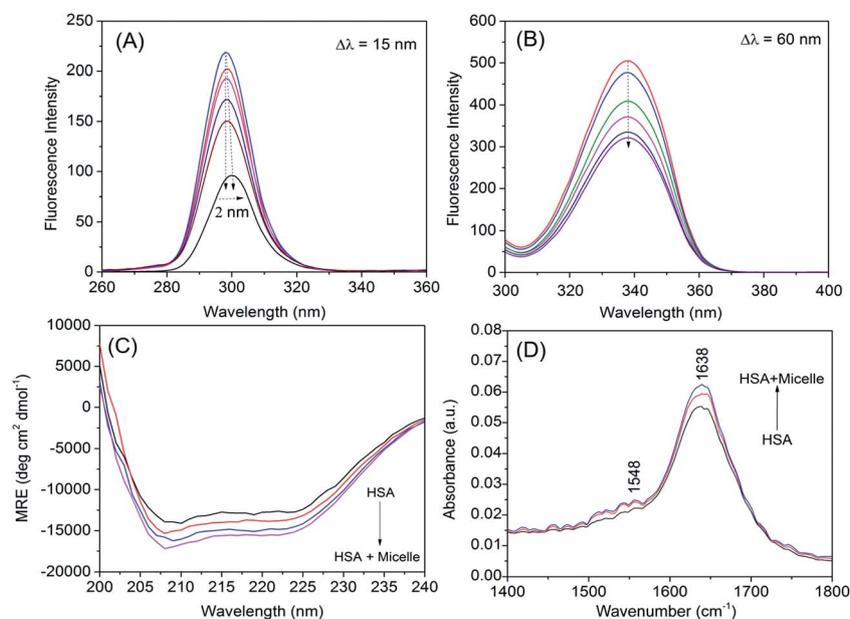

Fig. 7 Conformational change of human serum albumin induced by micelle. (A, B) Synchronous fluorescence spectra of HSA in the absence and presence of different concentrations of micelle (Δλ = 15 nm for tyrosine residues Δλ = 60 nm for tryptophan residue). (C) Far-UV CD spectra of HSA in the absence and presence of different concentrations of micelle. (D) Attenuated total reflection FTIR spectra of HSA and increasing concentrations of micelle (5 and 10 μg ml⁻¹) with HSA.
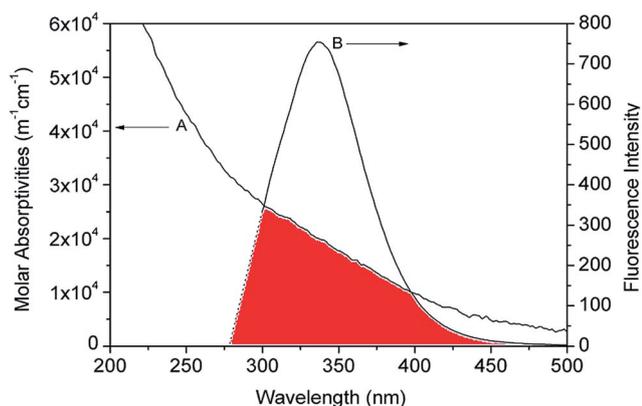
Fig. 8 Binding distance calculation by fluorescence resonance energy transfer. Overlap of absorption coefficient spectra of micelles (A) and the fluorescence emission spectrum of HSA (B). ([HSA] : [micelle] =1 : 1).

higher concentrations of micelle or the formation of an HSA–micelle complex *via* hydrogen bonding or hydrophobic interactions.[36]

Changes in protein secondary structure during interaction with other small molecules can also be analyzed by FTIR spectroscopy. Amide I and II frequencies of HSA are sensitive to such changes; the amide I band occurs in the region 1600–1700 cm^{-1} mainly due to C=O stretch, while the amide II peak occurs in the region of 1500–1550 cm^{-1} due to C–N stretch coupled with N–H bending.[37,38] The FTIR spectrum of HSA complexed with a micelle revealed no shifts in the amide I and II peaks, although their respective intensities increased (Fig. 7D), indicating that the secondary structure of HSA is slightly altered by interaction with micelles, consistent with the CD results.

3.5 FRET

The binding distance between donor–acceptor pairs can be calculated based on Förster non-radiative energy transfer. The
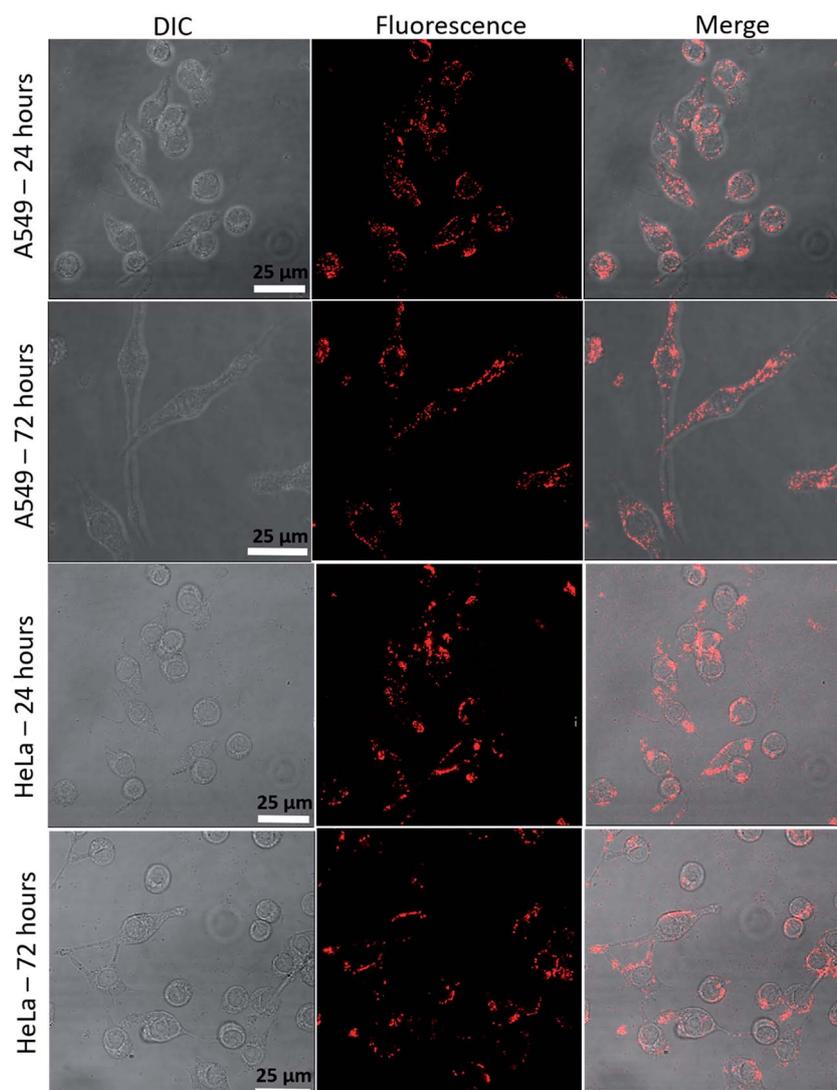

Fig. 9 Cellular uptake of micelles. HeLa and A549 cells were incubated with micelles for 24 or 72 h.

distance between HSA and the micelle is approximated by the distance between the Trp214 residue in the protein and the micelle surface. The rate of energy transfer depends on following factors: (i) the absorption spectrum of the acceptor overlaps with that of the donor; (ii) donor and acceptor molecules are separated by a distance of ≤2–8 nm; and (iii) the relative orientation of donor and acceptor transition dipoles. A significant overlap was observed between the emission spectrum of HSA and the absorption spectra of micelles (Fig. 8). According to the Förster theory of non-radiative energy transfer, the energy transfer efficiency, E, can be calculated as,[39,40]

$$E = 1 - \frac{F}{F_0} = \frac{R_0{}^6}{R_0{}^6 + r^6} \qquad (9)$$

where F and F_0 are the fluorescence intensity of HSA in the presence and absence of the micelle, respectively; r is the actual distance between donor and acceptor molecules; and R_0 is the critical distance when the efficiency is around 50% (ref. 41) – that is,

$$R_0 = 9.79 \, (K^2 N^{-4} \phi_{\mathrm{D}} J)^{1/6} \qquad (10)$$

here, K^2 is the spatial orientation factor between the donor and acceptor dipoles; $K^2 = 2/3$; N is the refractive index of the medium (1.336); ϕ is the quantum yield of the donor alone (0.118);[42] and J is the overlap integral of the emission spectrum of the donor and absorbance spectrum of the acceptor. According to the Förster theory, values of R_0, J, and E were calculated as 1.12 nm, 1.12×10^6 M^{-1} cm^{-1} nm^4, and 0.011, respectively. The value of r (= 2.37 nm) for the micelle was less than the theoretical range (~2–8 nm), indicating that the quenching of HSA by micelles is a non-radiative energy transfer process. As such, there is a high probability of FRET between protein and micelle.

3.6 Uptake of micelle-QDs by cancer cells

The uptake of QD micelles by cultured cancer cells was examined by confocal microscopy (Fig. 9). Within 24 h of exposure to micelles dissolved in HPLC water, cells accumulated micelles in the cell membrane and cytoplasm with high signal intensity. After 72 h of continuous incubation with micelles, the micelle fluorescence intensity from the cells was good. To verify cellular uptake of micelles, cells were harvested after 72 h of incubation with micelles using trypsin–EDTA solution and then reseeded. After an additional 72 h, fluorescence was observed in divided cells (Fig. S5†), indicating that QD micelles are highly stable in cancer cells and maintain both their micelle and fluorescence properties.

4. Conclusion

The present study described the properties and demonstrated the application of magneto-fluorescent CdSe/ZnS QD micelles for *in vitro* imaging and blood plasma protein binding studies. Even at a high concentration (25 μg ml⁻¹), micelles of various diameters were non-toxic to HeLa and A549 cells. We used 117.87 ± 2.55 nm-sized micelles for *in vitro* imaging, since

smaller particles are more readily taken up by cancer cells *via* blood vessels near the tumor site. In order to assess the potential for *in vivo* applications, we analyzed the interaction of micelles with the blood plasma protein HSA using different optical spectroscopic techniques. We found that the interaction was stabilized *via* hydrogen bonding, electrostatic forces, and hydrophobic interaction, with no obvious structural changes to the protein. Our findings indicate that CdSe/ZnS QD micelles can be useful for long-term imaging of biological samples by fluorescence microscopic methods.

Acknowledgements

References

1 W. A. W. Razali, V. K. A. Sreenivasan, C. Bradac, M. Connor, E. M. Goldys and A. V. Zvyagin, *J. Biophotonics*, 2016, **9**, 848–858.

2 M. X. Zhao, Y. Li, E. Z. Zeng and C. J. Wang, *Chem.–Asian J.*, 2014, **9**, 1349–1355.

3 D. Painuly, A. Bhatt and V. K. Krishnan, *Proceeding of International Conference on Recent Trends in Applied Physics and Material Science*, 2013, vol. 1536, pp. 63–64.

4 K. V. Zolotarev, V. N. Kashirtseva, A. V. Mishin, N. F. Belyaeva, N. V. Medvedeva and O. M. Ipatova, *ISRN Nanotechnol.*, 2012, **2012**, 1–5.

5 B. B. Manshian, S. J. Soenen, A. Al-Ali, A. Brown, N. Hondow, J. Wills, G. J. Jenkins and S. H. Doak, *Toxicol. Sci.*, 2015, **144**, 246–258.

6 S. Sanwlani, K. Rawat, M. Pal, H. B. Bohidar and A. K. Verma, *J. Nanopart. Res.*, 2014, **16**, 2382.

7 L. Peng, M. He, B. Chen, Q. Wu, Z. Zhang, D. Pang, Y. Zhu and B. Hu, *Biomaterials*, 2013, **34**, 9545–9558.

8 G. Amiri, A. Valipoor, K. Parivar, M. Modaresi, A. Noori, H. Gharamaleki, J. Taheri and A. Kazemi, *Int. J. Fertil. Steril.*, 2014, **9**, 512–520.

9 Y. J. Choi, Y. J. Kim, J. W. Lee, Y. Lee, Y. B. Lim and H. W. Chung, *J. Nanosci. Nanotechnol.*, 2012, **12**, 2160–2168.

10 J. Y. Zhao, L. M. Jia, W. Q. Song, W. L. Zhang, Y. M. Fu, Y. Zhang, W. W. Cao, Y. Sun, J. H. Zheng and F. M. Zhang, *J. Nanopart. Res.*, 2014, **16**, 2382.

11 W. Wang, Y. He, G. Yu, B. Li, D. W. Sexton, T. Wileman, A. A. Roberts, C. J. Hamilton, R. Liu, Y. Chao, Y. Shan and Y. Bao, *PLoS One*, 2015, **10**, e0138771.

12 J. Liu, F. Erogbogbo, K. T. Yong, L. Ye, J. Liu, R. Hu, H. Chen, Y. Hu, Y. Yang, J. Yang, I. Roy, A. Nicholas, N. A. Karker, M. T. Swihart and P. N. Prasad, *ACS Nano*, 2013, 7, 7303–7310.

13 F. Erogbogbo, K. T. Yong, I. Roy, R. Hu, W. C. Law, W. Zhao, H. Ding, F. Wu, R. Kumar, M. T. Swihart and P. N. Prasad, *ACS Nano*, 2011, **5**, 413.

14 F. Erogbogbo, K. T. Yong, R. Hu, W. C. Law, H. Ding, C. W. Chang, P. N. Prasad and M. T. Swihart, *ACS Nano*, 2010, **4**, 5131.

15 X. Peng, H. Fu, R. Liu, L. Zhao, Y. Zu, F. Xu and Z. Liu, *Scanning*, 2015, **37**, 158–164.

16 Kenry, K. P. Loh and C. T. Lim, *Nanoscale*, 2016, **8**, 9425–9441.

17 N. Fernandez-Iglesias and J. Bettmer, *Nanoscale*, 2015, **7**, 14324–14331.

18 T. Sen, S. Mandal, S. Haldar, K. Chattopadhyay and A. Patra, *J. Phys. Chem. C*, 2011, **115**, 24037–24044.

19 S. Tenzer, D. Docter, S. Rosfa, A. Wlodarski, J. Kuharev, A. Rekik, S. K. Knauer, C. Bantz, T. Nawroth, C. Bier, J. Sirirattanapan, W. Mann, L. Treuel, R. Zellner, M. Maskos, H. Schild and R. H. Stauber, *ACS Nano*, 2011, **5**, 7155–7167.

20 S. P. Boulos, T. A. Davis, J. A. Yang, S. E. Lohse, A. M. Alkilany, L. A. Holland and C. J. Murphy, *Langmuir*, 2013, **29**, 14984–14996.

21 D. Jung, S. Maiti, J. H. Lee, J. H. Lee and J. S. Kim, *Chem. Commun.*, 2014, **50**, 3044–3047.

22 S. Maiti, N. Park, J. H. Han, H. M. Jeon, J. H. Lee, S. Bhuniya, C. Kang and J. S. Kim, *J. Am. Chem. Soc.*, 2013, **135**, 4567–4572.

23 W. X. Ren, J. Han, S. Uhm, Y. J. Jang, C. Kang, J. H. Kim and J. S. Kim, *Chem. Commun.*, 2015, **51**, 10403–10418.

24 M. Banobre-Lopez, A. Teijeiro and J. Rivas, *Rep. Pract. Oncol. Radiother.*, 2013, **18**, 397–400.

25 A. C. Silva, T. R. Oliveira, J. B. Mamani, S. M. Malheiros, L. Malavolta, L. F. Pavon, T. T. Sibov, E. Amaro Jr, A. Tannus, E. L. Vidoto, M. J. Martins, R. S. Santos and L. F. Gamarra, *Int. J. Nanomed.*, 2011, **6**, 591–603.

26 K. Hayashi, M. Nakamura, W. Sakamoto, T. Yogo, H. Miki, S. Ozaki, M. Abe, T. Matsumoto and K. Ishimura, *Theranostics*, 2013, **3**, 366–376.

27 K. Hayashi, M. Moriya, W. Sakamoto and T. Yogo, *Chem. Mater.*, 2009, **21**, 1318–1325.

28 S. Chinnathambi, D. Velmurugan, N. Hanagata, P. R. Aruna and S. Ganesan, *J. Lumin.*, 2014, **151**, 1–10.

29 D. P. Yeggoni, A. Rachamallu and R. Subramanyam, *RSC Adv.*, 2016, **6**, 40225–40237.

30 D. Ray, A. Kundu, A. Pramanik and N. Guchhait, *J. Phys. Chem. B*, 2015, **119**, 2168–2179.

31 R. Sett, A. Ganguly and N. Guchhait, *J. Photochem. Photobiol., B*, 2016, **164**, 141–150.

32 R. Mangaiyarkarasi, S. Chinnathambi, P. Aruna and S. Ganesan, *J. Nanopart. Res.*, 2015, **17**, 136.

33 B. K. Paul, D. Ray and N. Guchhait, *Phys. Chem. Chem. Phys.*, 2013, **15**, 1275–1287.

34 P. D. Ross and S. Subramanian, *Biochemistry*, 1981, **20**, 3096–3102.

35 M. Wang, C. Fu, X. Liu, Z. Lin, N. Yang and S. Yu, *Nanoscale*, 2015, **7**, 15191–15196.

36 J. Wang, L. Ma, Y. Zhang and T. Jiang, *J. Mol. Struct.*, 2017, **1129**, 160–168.

37 Z. Q. Xu, Q. Q. Yang, J. Y. Lan, J. Q. Zhang, W. Peng, J. C. Jin, F. L. Jiang and Y. Liu, *J. Hazard. Mater.*, 2016, **301**, 242–249.

38 J. C. Ioannou, A. M. Donald and R. H. Tromp, *Food Hydrocolloids*, 2015, **46**, 216–225.

39 S. Chinnathambi, S. Karthikeyan, D. Velmurugan, N. Hanagata, P. Aruna and S. Ganesan, *Int. J. Spectrosc.*, 2015, **2015**, 1–12.

40 S. Chinnathambi, S. Karthikeyan, M. Keshervani, D. Velmurugan and N. Hanagata, *J. Phys. Chem. Biophys.*, 2016, **6**, 1–9.

41 S. Raut, R. Rich, R. Fudala, S. Butler, R. Kokate, Z. Gryczynski, R. Luchowski and I. Gryczynski, *Nanoscale*, 2014, **6**, 385–391.

42 Z. Cheng, R. Liu and X. Jiang, *Spectrochim. Acta, Part A*, 2013, **115**, 92–105.